Icarus 292 (2017) 1–12

Contents lists available at ScienceDirect

Icarus

journal homepage: www.elsevier.com/locate/icarus

Spatially resolved near infrared observations of Enceladus' tiger stripe eruptions from Cassini VIMS

Deepak Dhingra[a,*], Matthew M. Hedman[a], Roger N. Clark[b], Philip D. Nicholson[c]

[a] Department of Physics, University of Idaho, Moscow, ID 83844, USA
[b] Planetary Science Institute, 1700 East Fort Lowell, Suite 106, Tucson, AZ 85719, USA
[c] Cornell University, 418 Space Sciences Building, Ithaca, NY 14853, USA

ARTICLE INFO

Article history:
Received 4 July 2016
Revised 17 January 2017
Accepted 6 March 2017
Available online 14 March 2017

ABSTRACT

Particle properties of individual fissure eruptions within Enceladus' plume have been analyzed using high spatial resolution Visible and Infrared Mapping Spectrometer (VIMS) observations from the Cassini mission. To first order, the spectra of the materials emerging from Cairo, Baghdad and Damascus sulci are very similar, with a strong absorption band around 3 μm due to water-ice. The band minimum position indicates that the ice grains emerging from all the fissures are predominantly crystalline, which implies that the water-ice particles' formation temperatures are likely above 130 K. However, there is also evidence for subtle variations in the material emerging from the different source fissures. Variations in the spectral slope between 1–2.5 μm are observed and probably reflect differences in the size distributions of particles between 0.5 and 5 μm in radius. We also note variations in the shape of the 3 μm water-ice absorption band, which are consistent with differences in the relative abundance of >5 μm particles. These differences in the particle size distribution likely reflect variations in the particle formation conditions and/or their transport within the fissures. These observations therefore provide strong motivation for detailed modeling to help place important constraints on the diversity of the sub-surface environmental conditions at the geologically active south-pole of Enceladus.

1. Introduction

Enceladus' plume represents a direct sample from the moon's interior and therefore holds clues to the internal processes and the evolutionary history of this geologically active icy body. Enceladus' plume has been the focus of intense scientific analyses ever since it was discovered by the NASA-ESA Cassini mission (e.g. Dougherty et al., 2006; Spencer et al., 2006; Porco et al., 2006; Spencer and Nimmo, 2013). A diverse suite of instruments covering a wide range of the electromagnetic spectrum, as well as multiple in-situ measurements, have been employed in characterizing the plume's structure, composition, and the nature of its subsurface source (e.g. Waite et al., 2006; Hansen et al., 2006; Hsu et al., 2015; Ye et al., 2016). These observations have been complemented by theoretical modeling to understand the origin and character of the plume (e.g. Kiefer et al., 2006; Schmidt et al., 2008; Ingersoll and Ewald 2011) including the effects of tides, the presence of a global or regional ocean and the possible role of an impact event in initiating the plume activity at the south pole (e.g. Collins and Goodman, 2007; Nimmo et al., 2007; Hurford et al., 2007; Smith-Konter and Pappalardo, 2008; Iess et al., 2014; Nimmo et al., 2014; Roberts and Stickle, 2014; 2015).

Enceladus' plume is dominated by water vapor and ice grains and arises from individual eruptions along the four so-called "tiger stripe" fractures, named Damascus, Baghdad, Cairo and Alexandria. The water vapor composition of the plume was confirmed on the basis of in-situ measurements by the Ion and Neutral Mass Spectrometer (INMS) (Waite et al., 2006) and remote measurements by the Ultra-violet Imaging Spectrometer (UVIS) (Hansen et al., 2006). The particle component of the plume was based on the dust detection by the Cosmic Dust Analyzer (CDA) (Spahn et al., 2006; Postberg et al., 2008) as well as the Imaging Science Sub-system (ISS) (e.g. Porco et al., 2006). The dominantly water-ice composition of the plume particles was subsequently revealed by the Visual and Infrared Mapping Spectrometer (VIMS) instrument (Hedman et al., 2009) and the CDA instrument (Postberg et al., 2011). Analysis of the water-ice particles in the plume at different altitudes (50 km and above) by VIMS also revealed that there is a paucity of >3 μm particle sizes, especially at higher altitudes (Hedman et al., 2009). VIMS data is particularly valuable for investigations of the plumes' particle content because it can observe the light scattered by the

* Corresponding author.
E-mail address: deepdpes@gmail.com (D. Dhingra).

http://dx.doi.org/10.1016/j.icarus.2017.03.002
0019-1035/

plume particles over a broad range of wavelengths simultaneously, which places strong constraints on the particle size distribution. This is in contrast to the limited spectral range of ISS, which makes characterizing the physical and light-scattering properties of the grains more challenging (e.g. Ingersoll and Ewald, 2011; Dong et al., 2015; Gao et al., 2016). However, VIMS has a much lower spatial resolution than ISS (typically VIMS pixel sizes are 0.5 mrad) and so most of the time, it cannot discern the material launched from specific locations. Still, there are at least three sets of observations where VIMS has resolved individual fissure eruptions within the plume.

Here, we utilize these highest spatial resolution observations from the VIMS instrument to examine the properties of the materials erupting from individual source fissures (i.e. the tiger stripes fractures). This paper focuses on generating robust average spectra of the material coming from the individual fissures, identifying interesting spectral features and comparing these data with preliminary model spectra to identify potentially informative material properties. Fitting the observations to specific models in order to obtain quantitative estimates of the particle properties will require further analysis and so will be the subject of a separate paper. The general motivation for this work is to address the following questions: What is the compositional character of the plume across the individual source regions (fissures)? Are the properties of the water-ice particles similar along all the sources? If not, how do they differ and what could be the possible causes and implications?

In Section 2, we discuss the methods used for data reduction, background removal as well as details of the spectral modeling. In Section 3, we highlight interesting spectral characteristics of the plume as observed in VIMS observations and compare these with the low spatial resolution observations. Section 4 describes our first order interpretations of the spectral features and discusses further constraints obtained from spectral modeling. In Section 5, we describe the implications of our observations and modeling for the understanding of Enceladus' plume. In Section 6, we summarize the major results.

2. Data and methods

2.1. Observations and primary data reduction

This investigation makes use of three high spatial resolution VIMS observations obtained at high phase angles ($>140°$) and at distances between ~12,000 km and ~42,000 km from the center of Enceladus (corresponding to typical spatial resolutions between 6 and 24 km/pixel for VIMS) obtained between November 2009 and August 2010 during Cassini orbits ("Revs") 121, 131 and 136 (Fig. 1, Table 1).

In its standard imaging mode, VIMS uses two co-aligned instruments to acquire a series of visible and near-infrared spectra covering a scene. For this particular study, we focus our attention exclusively on the near-infrared data obtained by the VIMS-IR channel, which consists of a one-dimensional InSb array that can simultaneously measure the brightness of a given location in 256 wavelength bands between 0.85 and 5.2 µm. A two-axis scan mirror system allows this instrument to view a series of up to 64×64 locations in the sky to produce an image (see Brown et al., 2004 for more details about the instrument). We do not use data from the shorter-wavelength VIS channels primarily because of their lower signal-to-noise. It is challenging to co-align the visible and near-IR components of the faint plume observations, especially the high spatial resolution observations analyzed in this study. Further, we have restricted our analysis to 4 µm within the near-IR observa-

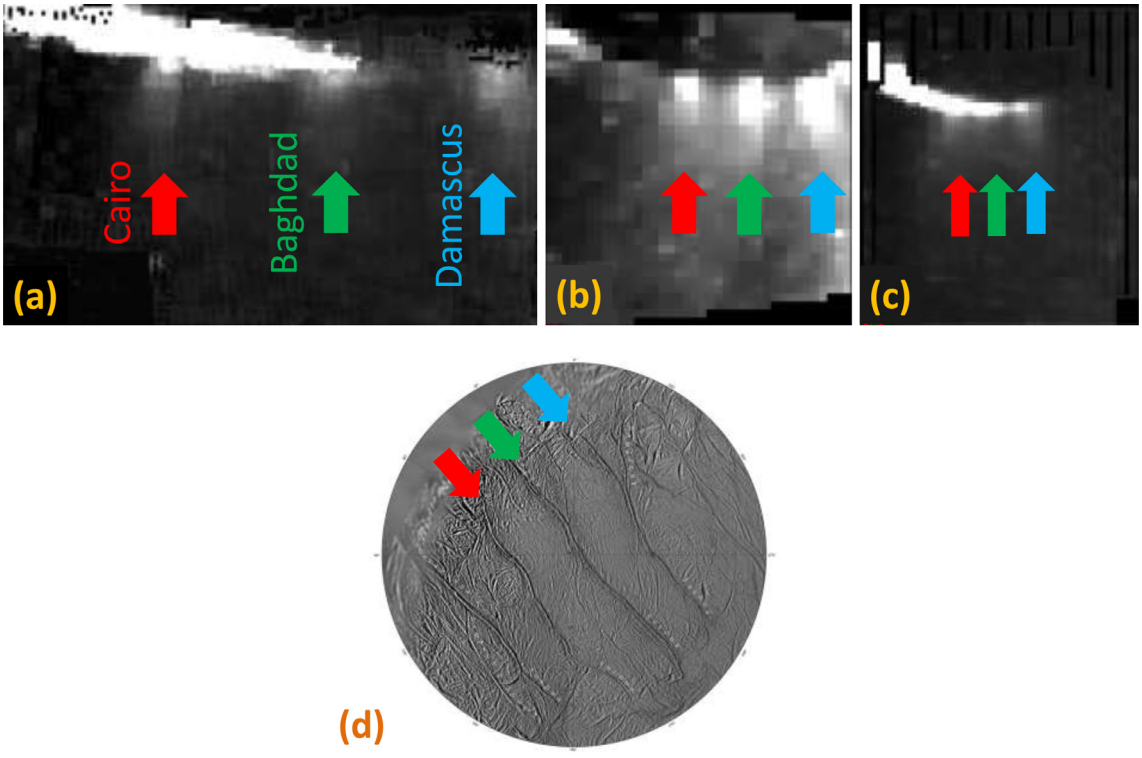

Fig. 1. High resolution VIMS maps of Enceladus' plume highlight spatially resolved eruptions along the tiger stripe fractures. All the maps are presented in the form of brightness images at 0.93 µm, and are oriented so the Enceladus' south-pole points downwards. (a) Map based on the spectral cubes from Rev 121 (The full map has been cropped for clarity). (b) Map from Rev 131 (c) Map from Rev 136. The material erupting from the individual tiger stripes is indicated with colored arrows. The bright crescent above the plume in (a) and (c) corresponds to the illuminated disc of Enceladus. Each image has been individually contrast stretched to highlight the fissure eruptions. (d) Geological context for the fissure eruptions is provided by this south polar mosaic of Enceladus based on ISS images (Image Source: http://ciclops.org/view/2441/The_Enceladus_Atlas). The fissures (from right to left) are Damascus, Baghdad and Cairo. (For interpretation of the references to colour in this figure legend, the reader is referred to the web version of this article.)

Table 1
The list of individual VIMS observations that were utilized to obtain the three spectral cubes in this study and shown in Fig. 1. For each set of cubes, the average distance between the spacecraft and Enceladus is provided along with the phase angle (Sun–Enceladus–Spacecraft angle) and orbital phase (angle between Enceladus' observed position and its orbital pericenter).

	Spectral cubes from Rev 121	Spectral cube from Rev 131	Spectral cubes from Rev 136
Component files	V1637460963	V1652853941	V1660424651
	V1637460999		V1660425166
	V1637461036		V1660425771
	V1637461144		V1660426015
	V1637461246		V1660426374
	V1637461348		V1660426972
	V1637461450		V1660427216
	V1637461544		V1660427573
	V1637461638		V1660427817
	V1637461728		V1660428174
	V1637461756		V1660428418
	V1637461846		
	V1637461907		
	V1637461968		
	V1637462045		
	V1637462106		
	V1637462167		
	V1637462228		
	V1637462289		
	V1637462350		
Spacecraft-Enceladus distance	12,000 km	17,000 km	42,000 km
Phase angle	144°	156°	154°
Orbital phase	143°	90°	42°

tions (instead of utilizing the full range extending to 5.2 μm) as the noise level increases dramatically at longer wavelengths. We have also removed data corresponding to known hot channels (1.24 μm, 1.33 μm, 3.23 μm, 3.24 μm, 3.83 μm) and IR focal plane blocking filters (1.6–1.67 μm, 2.94–3.01 μm and 3.83–3.89 μm) (Brown et al., 2004; Nicholson et al., 2008). The wavelength uncertainty associated with VIMS near infrared wavelengths is less than 10 nm or 0.01 μm [Roger Clark, pers. comm.]. As a result, the horizontal error bars in the spectral plots would be comparable to the size of the symbols in the plot.

Standard calibration routines were used to convert the raw data numbers into I/F, a standard measure of reflectance (the specific flux calibration being RC17, see Clark et al., (2012)). However, since the plume extends beyond Enceladus' surface, we cannot use standard tools like Integrated Software for Imaging Spectrometers (ISIS) to geometrically align and correct these data. Instead, we compute the instrument's line of sight for each pixel in each cube using the appropriate SPICE kernels (Acton, 1996). This line of sight is parameterized by two spatial coordinates (x and y) as illustrated in Fig. 2. The coordinates specify the location where the line of sight passes through the plane containing Enceladus' spin axis. In this frame of reference, north-pole is the positive y-axis and the south is the negative y-axis. Note that this plane is orthogonal to the line of sight's projection onto Enceladus' equatorial plane (Hedman et al., 2013). This reference frame is also used to estimate the plume's phase angle and its distance from the spacecraft.

The high-resolution data analyzed in this study were obtained during relatively close approaches to Enceladus, and so the observation geometry changes significantly over the several minutes required to take a single spectral cube. Hence, to facilitate the interpretation of these data we interpolated and re-projected the spectral data from each observation sequence onto a uniform grid of x and y values and have created a single spectral map of the plume from a given set of coordinated observations. Two of these maps (Fig. 1a, 1c) were generated from multiple cubes, while one map (Fig. 1b) was derived from a single cube covering the three tiger stripes. For convenience, the mosaicked spectral cubes are labeled using the associated Rev number (a number designating Cassini's orbit around Saturn when the observations were taken) of the observations.

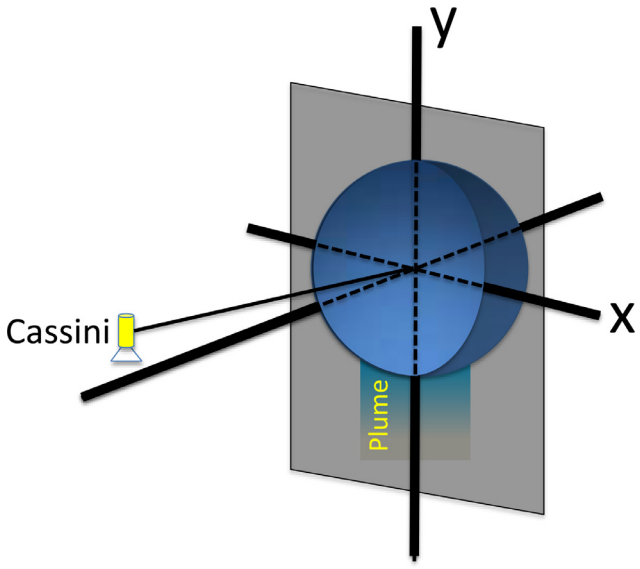

Fig. 2. Spatial reference framework for Enceladus' plume. The orthogonal axes X and Y lie in the plane that contains Enceladus' spin axis.

2.2. Background removal

While the plume material can be clearly seen in Fig. 1, the very low signal levels (peak I/F ~ 0.001) mean that careful background removal procedures are needed to obtain useful spectra. There are two main sources of the background: a) Instrumental and b) the E-ring. The E-ring consists of plume particles that escaped the moon's gravity and have gone into orbit around Saturn (e.g. Kempf et al., 2008; 2010). The E-ring is visible as a bright background in all the relevant VIMS datasets and has a spectral shape making it more challenging to remove. Since both the plume and the E-ring contain small water-ice particles, their spectra have similar basic shapes but there are known differences in their particle sizes (Spahn et al., 2006; Postberg et al., 2008; Hedman et al., 2009) which should impact the detailed spectral character.

We decided to subtract the background after the spectral cube mosaics were generated (instead of subtracting backgrounds from

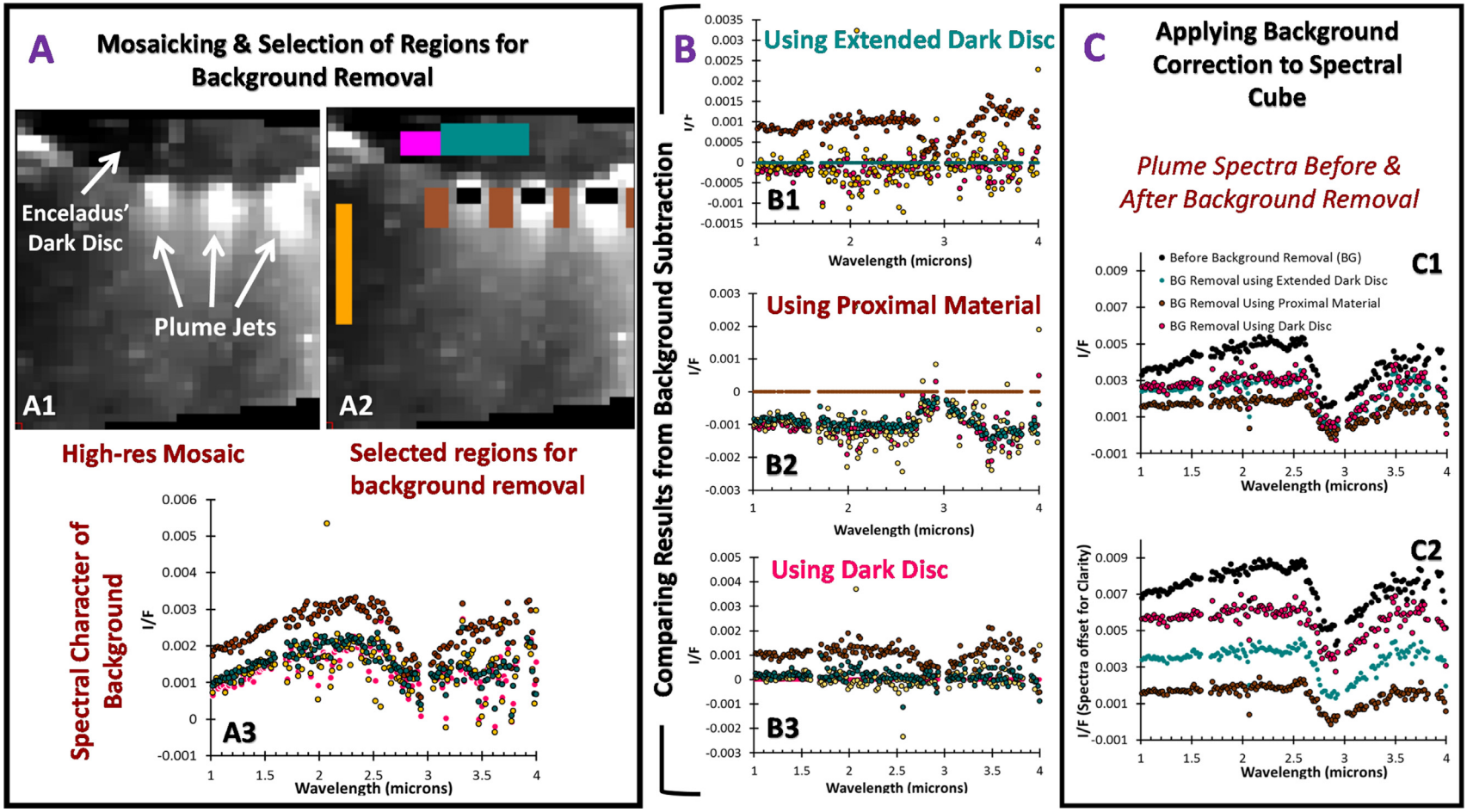

Fig. 3. Background removal methodology. A1) VIMS image mosaic (spectral cube 131) showing the spatially resolved eruptions. A2) Selected regions in the scene (magenta, teal, yellow, brown), located away from the plume are used for estimating the background. The black regions in A2 indicate the sampling locations for the plume material. A3) Spectral character of the background regions. B) Comparison of the results after background subtraction. C) Comparison of the spectral character of the plume material based on different backgrounds. Note that the background corrected spectra are broadly comparable, especially with respect to their band minimum position, which is critical for determining crystallinity. (For interpretation of the references to colour in this figure legend, the reader is referred to the web version of this article.)

Table 2
Regions selected for image-based background subtraction. The table provides the number of samples (x) and the number of lines (y) used for obtaining the average spectrum of each of the selected background regions in the three spectral mosaics. The notes refer to the color code used for the representation of different regions on the image cubes (see Figs. 3, 5, 9 and 10).

Spectral cube source Revs	Background location	X range(Samples)	Y range(Lines)	Notes
121	Bottom region	69:89	92:100	Yellow
	Proximal region to plume	31:51	43:60	Brown
		83:94	52:63	
		120:133	53:64	
131	Dark disc	15:19	13:15	Magenta
	Extended dark disc	20:30	12:15	Teal
	Proximal region to plume	18:20	20:24	Brown
		26:28	20:24	
		34:35	20:24	
		43:43	20:24	
	Left region	7:8	22:36	Yellow
136	Bottom region	25:56	75:78	Brown
	Left region	12:13	36:58	Yellow
	Top region	35:53	20:22	Teal

individual cubes). This was found to be a more practical approach considering the very small size of the individual spectral cubes from Revs 121 and 136. We computed the background for each spectral cube (Fig. 3) by selecting a region outside of the fissure eruptions and subtracting its average value from the entire mosaic/spectral cube. The standard deviation of the I/F values (at various wavelengths) for the selected background region was used as an estimate of the uncertainty for the spectral measurements. It should be noted that the background varies spatially, so we estimated the background using multiple locations and compared the background-removed spectra to make robust inferences. The details of the regions selected for estimating the background in all of the analyzed spectral cubes are provided in Table 2.

2.3. Mie-theory-based spectral modeling

We have compared the VIMS data with selected model spectra in order to explore potentially interesting spectral features. However, the low signal-to-noise properties of our data complicates efforts to fit them with models and to extract quantitative information. Accordingly, we use the model spectra for qualitative comparisons in this work. The model spectra were computed using a publicly-available Mie scattering code (source: http://eodg.atm.ox.ac.uk/MIE/mie_single.html). While Mie-theory calculations are only strictly valid for perfect spheres, they are still useful for exploring how parameters such as grain size, temperature of formation and ice phase (crystalline vs amorphous) affect the observed spectra. The code is inherently capable of generating a spectrum based on a *single particle size*. We added a peripheral code (wrapper) to this program to enable computation of the spectra for a *particle size distribution* in order to simulate the spectrum of the plume. The particle size distribution is based on a smooth interpolation between four discrete particle sizes provided by the user, similar to the one used by Hedman et al., (2009). The specific particle sizes used in the spectral modeling as well as the weighting scheme are discussed under spectral modeling results. We use optical constants of crystalline and amorphous ice from Mastrapa et al., (2008, 2009) in our spectral modeling effort.

3. Spatially resolved VIMS observations of tiger stripes eruptions

Most of the plume spectral observations by VIMS have been obtained at low spatial resolution where individual fissures cannot be sampled (see an example of bulk plume spectrum in Fig. 4a). The spatially resolved VIMS observations of the tiger stripes eruptions provide a unique opportunity to understand the contribution of individual fissure eruptions to the bulk plume spectra, as illustrated in Fig. 4b and c. In general, the high resolution data are consistent with the low spatial resolution observations but many subtle differences in the spectral slope and the shape of the 3 μm absorption band, observed between the individual fissure observations (Fig. 4c), are smeared and sometimes erased in the bulk plume spectra extracted from the same observations (Fig. 4b). These subtle spectral differences hold important clues about the plume properties and can be spectrally modeled to extract parameters such as crystallinity (amorphous vs crystalline) and band shape.

In all the three high spatial resolution VIMS spectral mosaics, we were able to easily identify and analyze the erupting material along Damascus, Cairo and Baghdad sulci (Fig. 1). However, jets over Alexandria could not be identified, possibly due to the relatively less intense particle eruptions there (Spitale and Porco, 2007; Porco et al., 2014). The results presented below are based on the collective insights gained from the analyses of the three spectral cubes. It should however be noted that the quality of data varies between the cubes. The spectral cube from Rev 131 exhibits the best quality spectral data and therefore has been used to identify and characterize the spectral trends across the three fissure eruptions. Spectral cubes from Revs 121 and 136 have relatively higher level of noise and were therefore used to only validate the observations from the Rev 131 cube. An average spectrum for each tiger stripe was computed by averaging over a selected set of pixels in each map (see Table 3).

We report three principal observations about the spectral character of the water-ice particles along the individual source fissure eruptions: (1) consistent band minimum position, (2) short wavelength (1–2.5 μm) spectral slope variations and (3) 3 μm band shape variations.

3.1. Consistent band minimum position

The band minimum position of the strong water-ice absorption band is observed to occur consistently long-ward of 2.8 μm across eruptions from all the three source fractures: Damascus, Cairo and Baghdad, and is independent of the chosen background (Fig. 5). The position of the band minimum is illustrated for one set of spectra (from Rev 131) in Fig. 4b and c using polynomial fits (order 6) to the water-ice band. This observation is also validated by the spectral cubes from Revs 121 and 136 (see Appendix). In addition, our recent analysis of more than 30 low spatial resolution VIMS

Table 3
Regions selected for sampling of the fissure eruptions. The table provides the number of samples (x) and the number of lines (y) averaged to obtain the spectra over each of the fissure regions (Cairo, Baghdad and Damascus) in the three spectral image cubes. The notes refer to the color code used for the representation of different regions on the image cubes in Figs. 5, 9 and 10.

Spectral cube source Revs	Plume region	X range(Samples)	Y range(Lines)	Notes
121	Cairo	62:68	47:52	Red
	Baghdad	102:108	48:53	Green
	Damascus	140:152	47:52	Blue
131	Cairo	22:24	20:21	Red
	Baghdad	30:32	20:21	Geen
	Damascus	38:41	20:21	Blue
136	Cairo	26:30	35:36	Red
	Baghdad	33:36	35:36	Green
	Damascus	43:45	35:36	Blue

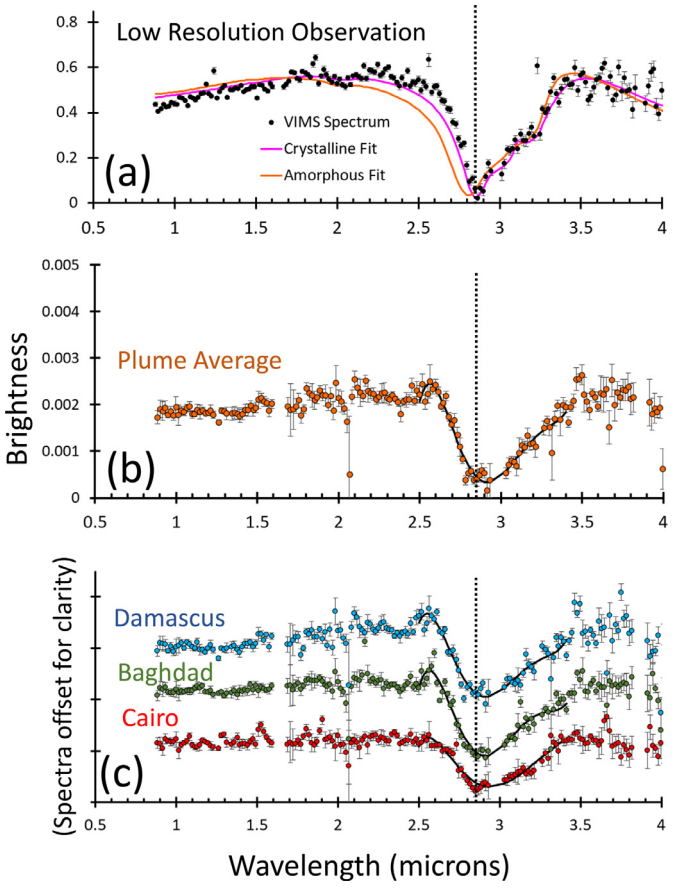

Fig. 4. Spectral comparison of the low spatial resolution plume observations and spatially resolved spectra of individual fissure eruptions. (a) Low resolution VIMS observation (black circles) of the plume (spectral cube 3 from Hedman et al., 2009). The spectra was sampled at an altitude of about 40 km above the surface. Mie-theory-based modeling favors a crystalline nature (magenta spectrum) for the plume water-ice particles instead of the amorphous nature (orange spectrum). Note that the model spectra have been scaled to match the brightness levels of the observations. The brightness in this case is horizontally integrated. (b) A simulated low resolution observation generated by averaging the high spatial resolution observations (from Rev 131) shown in c. (c) Spectra from the same spectral cube as in (b) but representing the spectral character of the individual tiger stripes. Note that many spectral features observable here are either subdued or erased in the averaged spectra shown in (b). The dotted line at 2.85 μm is provided as a common reference to enable comparison of band minimum position across different spectra in various spectral plots in the figure. Polynomial fits (order 6) to the water-ice absorption band near 3 μm are overlain on the high spatial resolution spectra to indicate their approximate band minimum positions. Vertical error bars are a measure of statistical errors derived from the scatter in the data from background regions. (For interpretation of the references to colour in this figure legend, the reader is referred to the web version of this article.)

spectral observations of the plume further confirms this spectral character for the bulk plume material (namely, water-ice band minimum position beyond 2.8 μm) (Dhingra et al., 2015). This spectral property is an evidence for the dominantly crystalline character of the water-ice particles and has been effectively demonstrated by spectral modeling (see Vahidinia et al., 2011 and Section 4 below). The crystalline character of the water-ice particles has implications for their formation mechanism and subsurface environmental conditions (see Section 5).

3.2. Short wavelength (1–2.5 μm) spectral slope variations

Subtle differences in the spectral slope between 1–2.5 μm can be observed in Fig. 5 (namely, 5c, 5d and 5 g) for the water-ice particle eruptions along the three source fissures. The spectral slope for Damascus is distinctly redder while spectral slope of the particle eruptions over Cairo is almost flat. These differences are independent of the chosen background. We note that the absolute magnitude of the spectral slope differences vary when compared with the observations from cubes from Revs 121 and 136. In principle, spectral slope differences could reflect subtle variations in the E-ring and instrumental backgrounds across fissures. However, since the relative slope differences are still maintained across different chosen backgrounds and are also noted in different observations, they are more likely to reflect real differences in the character of the three fissure eruptions.

We also carried out a quantitative assessment of the slope variations between the three fissure eruptions to obtain a first order constraint on their magnitude. A linear fit was applied to each of the spectrum between 1–2.45 μm to extract the spectral slope. Subsequently, residuals between the linear fit and the data were used to estimate the uncertainty associated with the slope (Table 4). Finally, the I/F values (derived from the linear fit) for all the three fissure eruptions were normalized to unity at 1 μm (Fig. 6) to enable a direct comparison of the slope differences at short wavelengths (1–2.45 μm).

Another interesting observation is the steep change in slope, in the form of a sharp peak, near the short wavelength edge of the strong 3 μm water-ice absorption (2.4–2.6 μm). This feature is prominently observed in the spectra from Damascus and Baghdad but is absent in the spectra from Cairo eruptions (see the dotted box in Fig. 5d, f, and h). This observation is independent of the background correction. One possible explanation for this sharp peak is that it might be arising from the strongest H_2O gas emission feature (ν_3) at 2.69 μm, which is superposed on the water-ice absorption band (e.g. Crovisier, 1984; Bockelée-Morvan et al., 2015; Debout et al., 2016; Gianrico Filacchione and Allesandra Migliorini, Pers. comm.). In view of the limited data and information, this observed feature could also have some other origin and so the detailed analysis of this feature must be the subject of future work. Still, the fact that the occurrence of this feature varies among the

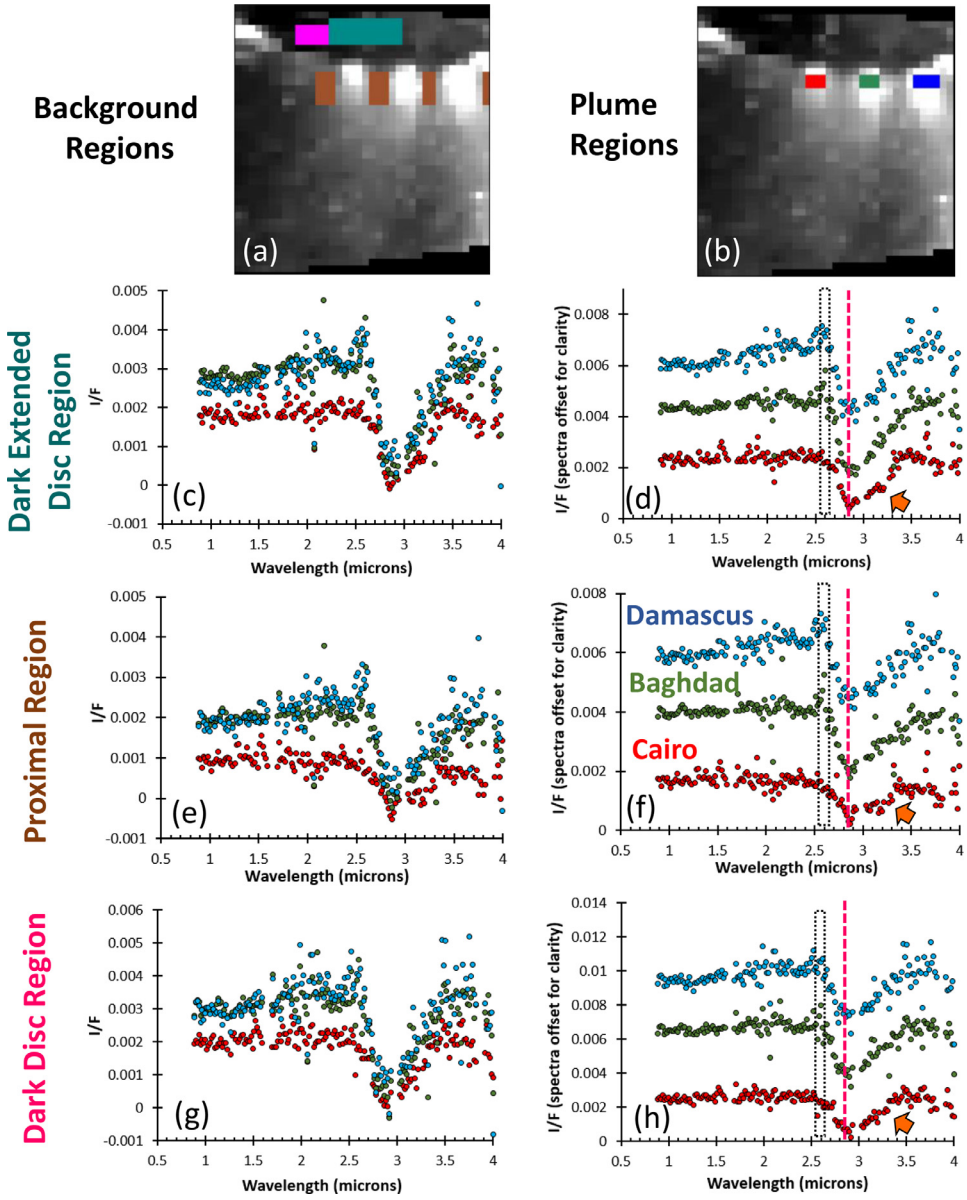

Fig. 5. Spectral character of the eruptions along Baghdad, Cairo and Damascus sulci. Brightness image (0.93 μm) from spectral cube from Rev 131 showing regions sampled for (a) background removal and (b) fissure eruptions. (c) Plume spectra based on background subtraction using the extended dark disc. (d) Same spectra offset for clarity. (e) Plume spectra based on background subtraction using the proximal regions. (f) Same spectra offset for clarity. (g) Plume spectra based on background subtraction using the dark disc. (h) Same spectra offset for clarity. The magenta dotted line indicates the approximate band minimum position and highlights the crystalline character of the water-ice grains. The orange arrow shows the inflection in Cairo spectrum. Spectra from Damascus and Baghdad seem to lack this feature. The dotted box around 2.6 μm highlights a spectral peak, observed in the case of eruptions along Damascus and Baghdad but not at Cairo. Errors on the data points are the same as those shown in Fig. 4c, and are not included for the sake of clarity. (For interpretation of the references to colour in this figure legend, the reader is referred to the web version of this article.)

Table 4
Estimated short wavelength (1–2.5 μm) spectral slope and associated uncertainties for the individual fissure eruptions shown in Fig. 5 (spectra in 5c).

Fissure eruption	Spectral slope ± Error	Offset ± Error	(Spectral slope ± Error) / Estimated brightness at 1 μm
Cairo	$(10 \pm 4) \times 10^{-5}$	$(171 \pm 7) \times 10^{-5}$	0.0554 ± 0.021
Baghdad	$(25 \pm 4) \times 10^{-5}$	$(257 \pm 6) \times 10^{-5}$	0.0890 ± 0.012
Damascus	$(58 \pm 5) \times 10^{-5}$	$(187 \pm 8) \times 10^{-5}$	0.2376 ± 0.019

tiger stripe fissure eruptions, provides further evidence for spectral differences within the plume.

3.3. 3-Micron band shape variations

We also note subtle differences in the shape of the 3 μm absorption band across Damascus, Baghdad and Cairo sulci (best illustrated in Fig. 5d) with the former two having similar band shapes characterized by a smoothly transitioning (gently sloping) band that exhibits relatively steeper slope at shorter wavelengths but gentler slope at longer wavelengths. Particle eruptions along the Cairo fracture however, seem to display an inflection around 3.2 μm (orange arrow in Fig. 5d), which is not observed in eruptions over Damascus or Baghdad. As a result, the absorption band at Cairo is wider (has larger band area) and is more asymmetric.

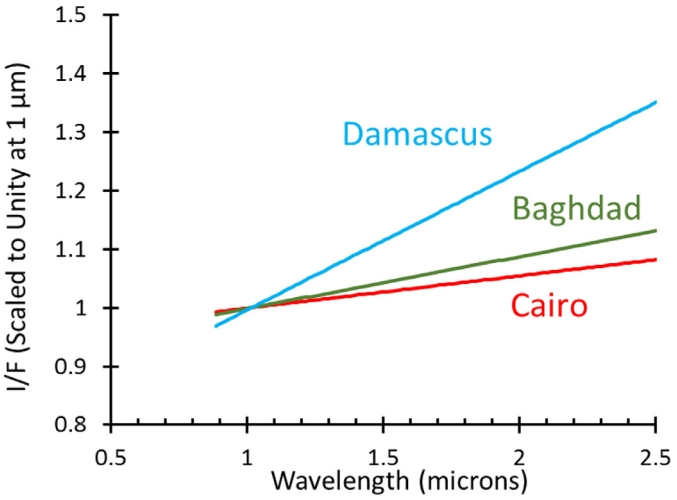

Fig. 6. Estimated short wavelength (1–2.5 μm) spectral slope differences between individual fissure eruptions, shown in Fig. 5 (spectra in 5c). The I/F values have been scaled to unity at 1 μm to enable direct comparison of the slope differences (without being affected by different offsets).

The shape of this inflection feature in the Cairo spectrum depends on the type of background subtraction that has been applied. The inflection is observable when either the extended dark disc or proximal regions are used for background subtraction (Fig. 5d, and f). However, no observable inflection is observed when dark disc region based background subtraction is carried out. The spectral cubes from Revs 121 and 136 (see appendix) are too noisy around 3.2 μm to provide additional information about this particular observation. This highlights the challenge faced in the identification of such subtle spectral features in noisy spectra. Meanwhile, in a separate analysis of low spatial resolution observations of the plume, where individual fissure eruptions cannot be resolved, we have also observed a similar inflection around 3.2 μm in many observations (Dhingra et al., 2015, 2016). In view of the repeated occurrence of the 3.2 μm feature in numerous observations at different spatial resolution, we have carried out spectral modeling (see Section 4.2) to explore the potential cause of this feature.

4. Interpretation of spectral features

In order to better constrain our spectral observations of the water-ice eruptions, we modeled the contribution of various physical parameters to the water-ice spectrum. The wavelength range of VIMS is similar to the size range of the water-ice particles in the plume and therefore it requires the modeling to be carried out within the framework of the Mie theory (e.g. Brown et al., 2008,2016). The physical parameters considered in the modeling include particle size distribution, temperature of formation and amorphous vs crystalline phase of water-ice. Following Hedman et al., (2009), we assume that the particle size distribution has the form $dn/ds = s^{-3}$ W(s), where W(s) is a weight function that smoothly interpolates between a set of specified particle sizes. For the high-phase-angle observations considered here, there is a rather direct relationship between the observed brightness trends and particle size, and so varying W(s) has relatively predictable and direct effects on the modeled spectra. The modeling results have subsequently been compared with the observations in Section 5.

4.1. Effect of crystalline vs amorphous phase on the position of band minimum

The position of the 3 μm band minimum is sensitive to whether the water-ice is crystalline or amorphous (e.g. Mastrapa et al., 2009). We evaluated the spectral character of the ice phases (crystalline and amorphous) at different temperatures. In general, the band minimum position of amorphous water-ice occurs at shorter wavelengths compared to the crystalline ice (Fig. 7). We note that there is also a detectable change in the band minimum position of amorphous ice with respect to temperature (15 – 120 K). The band minimum position shifts to longer wavelengths with an increase in temperature, consistent with previous work (e.g. Mastrapa et al., 2009). In contrast, the shift in band minimum for crystalline water-ice does not vary much over the same temperature range.

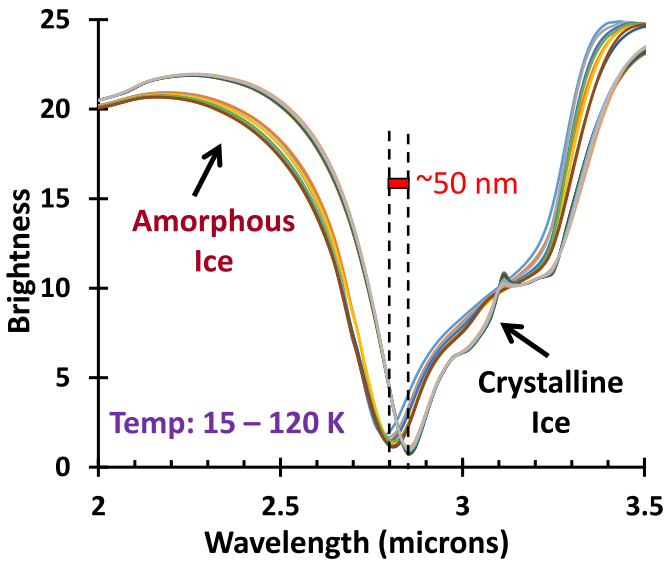

Fig. 7. Spectral modeling of water-ice phases. Model spectra of amorphous and crystalline ice show differences in the band minimum position with ice phase and at different temperature. However, note that the relative differences in the band minimum position between crystalline and amorphous ice is still maintained highlighting the utility of this parameter in distinguishing between the two phases of ice. We used weighting values of 0,1,1,0 for the particle sizes 1, 2, 3 and 4 μm respectively, following the procedure of Hedman et al., (2009). The phase angle was 160°.

Based on this spectral modeling, there is a difference of ~50 nm between the band minimum position of crystalline and amorphous ice phases, which can be easily resolved by Cassini VIMS observations with sampling of 16.6 nm. It should be noted that for the small grains that dominate the plume signal, crystallinity is by far the most important parameter, with particle size and temperature being secondary (e.g. Vahidinia et al., 2011). This is in contrast to the scattering signal from larger particles (where particles are several times the interacting wavelength), in which case, all the three parameters can significantly affect the location of the band minimum.

4.2. Effect of particle size on band shape and spectral slope

We used different particle size distributions (see Table 5) to evaluate their effect on the shape of the 3 μm water-ice absorption band for the case of crystalline ice. As explained earlier, the particle size distribution used in the modeling has the form $dn/ds = s^{-3}$ W(s), where W(s) is a weight function. We used weighting values of 0,1,1,0 for four specified particle sizes. The factors like [0, 1, 1, 0] are multiplicative in nature, on top of an s^{-3} power law, which is then interpolated at intermediate particle sizes. The obtained model size distribution has a peak near the median of the specified particle sizes, and a width given by the difference between the second and third particle sizes.

The computed model spectra reveal several interesting trends. Relatively fine-grained and narrow particle size distribution generally gives rise to gently sloping wings in the interior of the 3 μm

Table 5
The parameters used in generating the spectra in Fig. 8 to illustrate the effect of grain size on the shape of 3 μm band. Paucity of grain sizes less than 2 μm (#6, #7, #8) seem to have a dramatic effect on the shape of the 3 μm band, especially at longer wavelengths. W(s) is a weight function that specifies the shape of the particle size distribution.

Spectra	Particle radius (microns)	Distribution (Weight)	Comments
1.	1, 2, 5, 8	0, 1, 1, 0	Small + Large particle sizes, Wider range
2.	1, 2, 4, 6		
3.	1, 3, 6, 7		
4.	1, 2, 3, 4		Small Particle sizes, Narrower range
5.	1, 2, 2.5, 3.5		
6.	2, 4, 6, 7		Increasingly larger particle sizes, Wide range
7.	2, 5, 7, 9		
8.	3, 6, 8, 10		

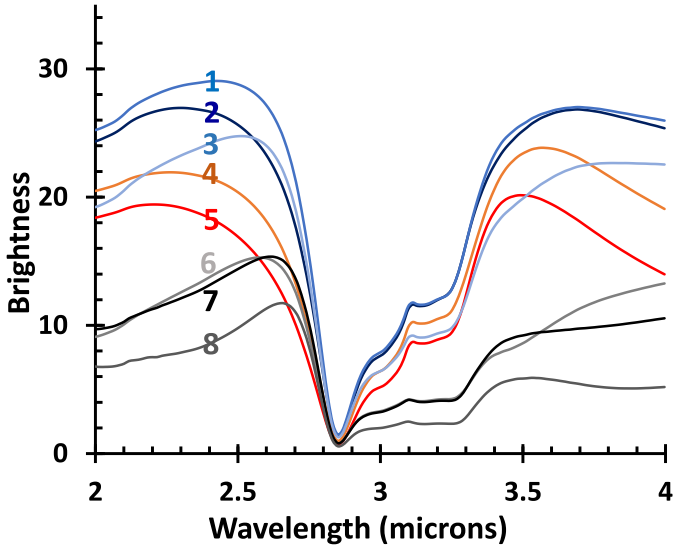

Fig. 8. Assessment of the particle size effects on the shape of 3 μm water-ice absorption band for crystalline ice. We used weighting values of 0,1,1,0 for each group of selected particle sizes following the procedure of Hedman et al., (2009). The spectra correspond to a formation temperature of 100 K and scattering angle of 20° (phase angle of 160°). The particle sizes used for each of the spectra are provided in Table 5 below. Spectra over the entire wavelength range (1–4 μm) are presented in the supplementary figure S1. (For interpretation of the references to colour in this figure legend, the reader is referred to the web version of this article.)

absorption band at both short and long wavelengths (Fig. 8, #4, #5). These absorption band slopes on both sides become increasingly steep with the addition of larger grain sizes, making the absorption band relatively narrow but only up to a certain threshold (Fig. 8, #1, #2, #3). For even larger particle sizes, the long wavelength wing becomes increasingly flatter in slope, in contrast to the still steep slope of the short-wavelength section of the absorption band (Fig. 8, #6, #7, #8). In addition, an inflection between 3.2–3.3 μm becomes increasingly prominent, making the absorption band very asymmetric and distorted. Although not an exact match, this inflection closely resembles our earlier observations of such a feature in the VIMS spectra of Cairo eruptions (marked by orange arrow in Fig. 5d, f, and h).

We also note slope differences immediately outside of the absorption band (i.e. the absorption band wings) that could be useful in interpreting remotely obtained spectral data. Smaller particles with a narrow range have a flatter trend at shorter wavelengths (< 2.6 μm) and a steeper trend immediately outside the absorption band at longer wavelengths (> 3.5 μm) (Fig. 8; spectra #4, #5). The trend is reversed with the addition of slightly larger particles. The slopes become steeper at shorter wavelengths outside of the absorption band while the flatter trend is observed at longer wavelengths. It should be noted that these trends are based on a limited set of iterations and many other possibilities may exist. However, the trends provide a fair idea about the nature of changes that take place with differences in the particle size distributions and are therefore very helpful in the interpretation of VIMS observations made here.

In the context of VIMS observations, the short-wavelength (1–2.5 μm) spectral slope differences between the fissures eruptions (Damascus having a distinctively redder slope compared to Cairo) are interpreted to be due to the corresponding differences in their respective particle size distributions. It should be noted here that although VIMS has so far only detected water-ice particles in the plume, there is evidence for the presence of organic particles in the plume from other instruments (e.g. Postberg et al., 2011). Accordingly, apart from the water-ice particles, these organic particles may also have a role to play in the observed spectral slope variations between individual fissure eruptions.

5. Discussion

The analyses of spatially resolved eruptions along individual fissures have provided new insights about the character of Enceladus' plume. This information has important implications for the understanding of subsurface environmental conditions as well as their variability along the source fissures.

5.1. Dominantly crystalline character of the water-ice particles

The spectral analysis of water-ice particles along different source fissures and across multiple observations suggest a dominantly crystalline character based on the 3 μm band minimum position (Figs. 5, 7, 9 and 10). Our modeling results for the water-ice particles (under a variety of conditions) further constrain the crystalline character of water-ice, indicating that the band minimum position of crystalline ice is always located long ward in wavelength (> 2.8 μm) with respect to the amorphous ice. The crystalline nature of the ice places constraints on the formation conditions of the ice particles. The ice grains are thought to form by some combination of vapor condensation (Schmidt et al., 2008) and flash freezing of liquid droplets (e.g. Porco et al., 2006; Postberg et al., 2011). Crystalline ice is only expected to form from condensing vapor at temperatures above 130 K (e.g. Hobbs, 1974), although it can form at lower temperatures if the gas flux is sufficiently low or the pressure is high (Kouchi et al., 1994). The generally warmer temperatures (> 130 K), required for the formation of crystalline ice, are consistent with the VIMS-based temperature measurements (~ 200 K) along one of the tiger stripe fractures, using spatially resolved thermal emission at near infrared wavelengths (Goguen et al., 2013).

5.2. Sub-surface environmental variables are largely spatially uniform

Our spectral models show that relatively small variations in the mean grain size can produce detectable changes in the spectral

slopes and band shape. Considering the fact that the plume activity along the fissures is spread across a very large region (several tens of kilometers), it is conceivable to have variations in parameters like the vent geometry, sub-surface temperature gradient, supply from the reservoir and formation path length of these particles which could potentially lead to differences in the particle properties (e.g. Schmidt et al., 2008). Hence, it is somewhat surprising that the spectra of the material emerging from the different fissures are so similar. These observations indicate that any variations in the physical setting are actually quite modest.

5.3. Evidence for subtle spectral variability

Although the water-ice particle characteristics in the individual fissure eruptions are relatively uniform, we do note some subtle (but potentially important) differences based on the analysis carried out so far. The presence of an inflection around 3.2–3.3 μm in the spectra of the eruptions along Cairo is distinct from the spectral character of the water-ice particles at Baghdad and Damascus. Based on our modeling studies, we interpret this difference in the band shape characteristics to be consistent with the production of relatively larger ice particles (> 5 μm) along the Cairo fracture. Although it would be desirable to evaluate the spectral variability with altitude or across any given eruption, the same is difficult to assess due to signal-to-noise constraints. However, on the basis of an on-going study, we have also reported band shape variations in the integrated plume observations obtained at low spatial resolution (Dhingra et al., 2016), providing independent evidence for band shape differences in the 2.8 μm water-ice absorption. Since the band shape differences are observable even at the scale of the entire plume (rather than between individual fissure eruptions contributing to the plume), these differences potentially hold important clues about the inner workings of the plume.

The band shape differences, together with the observed differences in the short wavelength (1–2.5 μm) spectral slope are likely linked to the differences in the grain size distribution across various fissure eruptions. If true, it raises an important question about the possible cause of these differences in grain size distribution. It is conceivable that the conditions within each tiger stripe may be different and may be affecting the particle formation and transport processes (which would then impact the particle size). Accordingly, each fissure eruption may need to be treated (and understood) separately. The exact cause of possibly different grain size distributions along tiger stripe fissures is however, still an open question because of our lack of clear understanding about the formation process of the ice particles in the plume: Are all ice particles forming directly from liquid water? Are all the particles individual grains or some of them aggregate together to form larger particles (e.g. Gao et al., 2016)? Is there a contribution from the icy walls? If yes, what is the abundance and size distribution of those particles? Investigation of these different possibilities would require several focused future studies.

6. Summary and conclusions

This work provides the first near-infrared look into the character of eruptions along each of the tiger stripe source fissures. We utilize the near-infrared range of the VIMS instrument to probe the spectral character of the water-ice particles in the eruptions and also model the spectra by varying environmental variables including temperature, particle size and distribution. The major conclusions from this study are as follows:

(i) We find that the water-ice particles are dominantly crystalline in character and accordingly infer that the subsurface

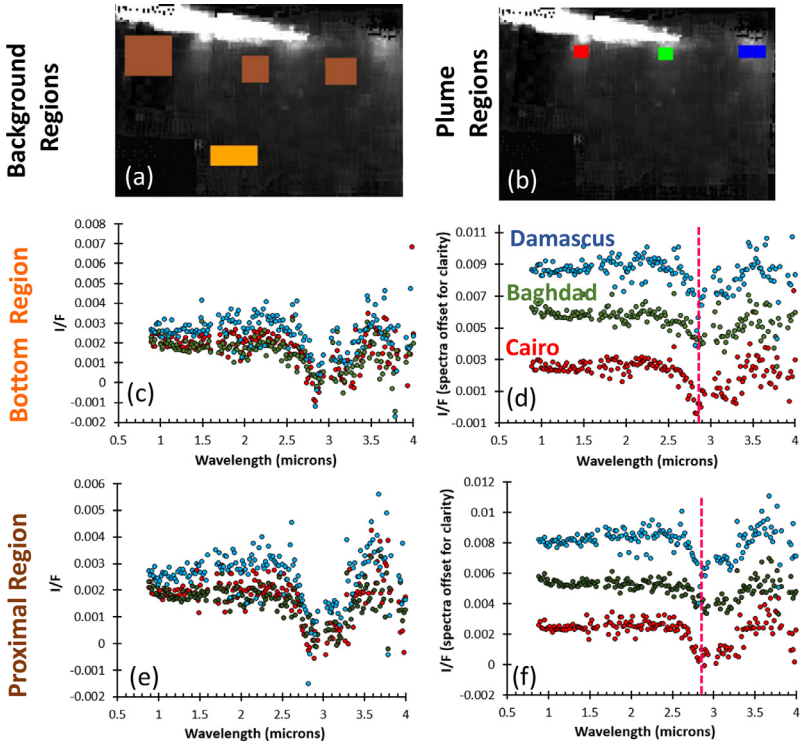

Fig. 9. Spectral character of the eruptions along Baghdad, Cairo and Damascus sulci. Brightness image (0.93 μm) from spectral cube from Rev 121 showing regions sampled for (a) background removal and (b) fissure eruptions. (c) Plume spectra based on background subtraction using the bottom region. (d) Same spectra offset for clarity. (e) Plume spectra based on background subtraction using the proximal regions. (f) Same spectra offset for clarity. Magenta dotted line at 2.85 μm is drawn to serve as a reference for comparison of the approximate band minimum position. (For interpretation of the references to colour in this figure legend, the reader is referred to the web version of this article.)

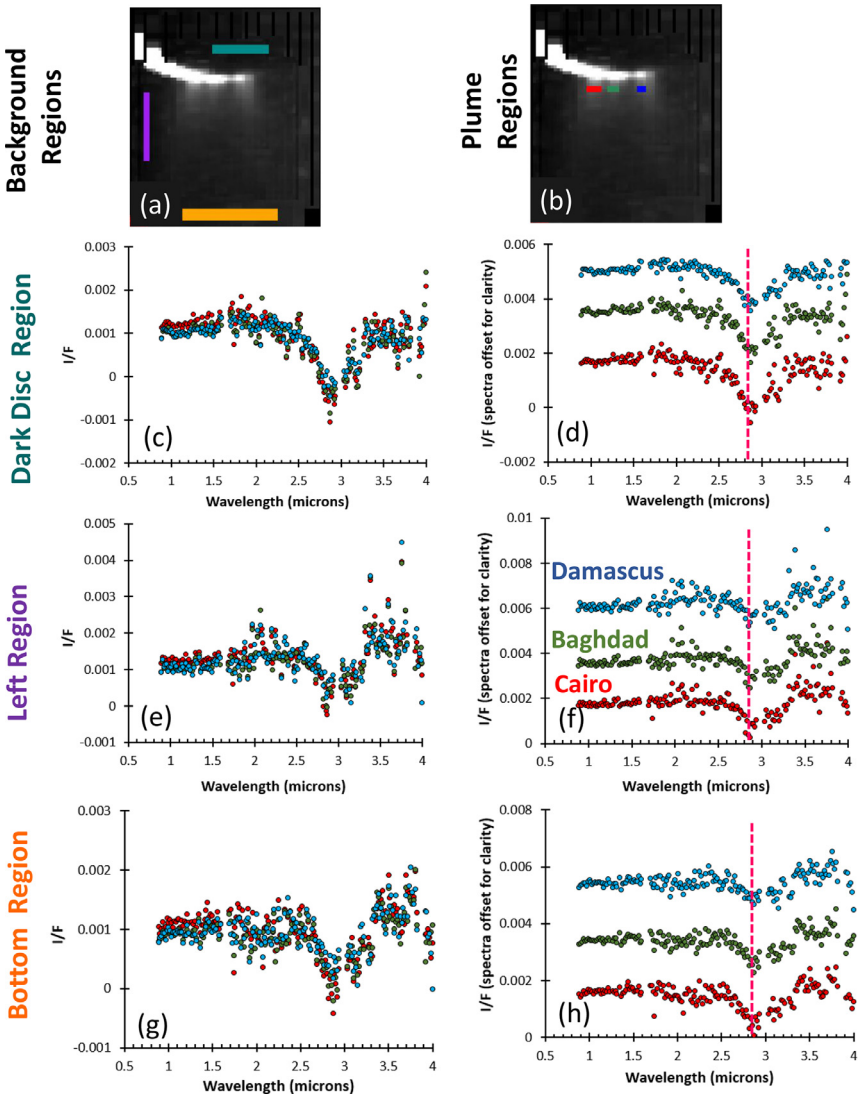

Fig. 10. Spectral character of the eruptions along Baghdad, Cairo and Damascus sulci. Brightness image (0.93 μm) from spectral cube from Rev 136 showing regions sampled for (a) background removal and (b) fissure eruptions. (c) Plume spectra based on background subtraction using the dark disc. (d) Same spectra offset for clarity. (e) Plume spectra based on background subtraction using the left region. (f) Same spectra offset for clarity. (g) Plume spectra based on background subtraction using the bottom region. (h) Same spectra offset for clarity. Magenta dotted line at 2.85 μm is drawn to serve as a reference for comparison of the approximate band minimum position. (For interpretation of the references to colour in this figure legend, the reader is referred to the web version of this article.)

formation temperature of these particles is likely greater than 130 K.

(ii) Our analysis highlights the remarkable uniformity in the character of the water-ice particles which is striking compared to the large spatial extent of the eruptions, and may indicate that the vents and their immediate subsurface regions have broadly similar properties.

(iii) This work also highlights subtle but important differences in the spectral properties of water-ice particles erupting from the tiger stripe fractures. We interpret Cairo's distinctive 3 μm band shape to be consistent with the presence of relatively larger particles (> 5 μm) in the eruptions from that fissure, and the redder slopes in Baghdad and Damascus, between 1 and 2.5 μm, due to the paucity of smaller size water-ice grains (< 2 μm) compared to the larger grain population (~2–3 μm) erupting along these fissures. The observed spectral peak (at 2.6–2.7 μm) in the Damascus and Baghdad eruptions and its absence in Cairo eruptions is another subtle difference that may be important.

This study thus provides several new inputs for modeling the formation of the giant geysers at Enceladus and in understanding the dominant controls of the formation process of the particle component of the plume.

7. Appendix

The spectra of the individual fissure eruptions from spectral mosaics from Revs 121 and 136 (Figs. 9 and 10, respectively) provide additional support for the observations made based on spectral cube from Rev 131 despite the fact that the two mosaics (#121 and #136) have relatively low signal to noise.

Acknowledgments

This work was partially supported by Cassini Data Analysis Program Grant NNX14AO27G. We thank NASA, the Cassini Mission and the VIMS Team for producing the data used in this analysis. We wish to thank Gianrico Filacchione and Allesandra Migliorini for

helpful discussions regarding the occurrence of H_2O emission in the near infrared spectra of the plumes. We sincerely acknowledge the thoughtful comments and suggestions by the two anonymous reviewers.

Supplementary materials

Supplementary material associated with this article can be found, in the online version, at doi:10.1016/j.icarus.2017.03.002.

References

Acton, C.H., 1996. Ancillary data services of NASA's navigation and ancillary information facility. Planet. Space Sci. 44 (1), 65–70.

Bockelée-Morvan, D., Debout, V., Erard, S., Leyrat, C., Capaccioni, F., Filacchione, G., Fougere, N., Drossart, P., Arnold, G., Combi, M., Schmitt, B., Crovisier, J., de Sanctis, M.-C., Encrenaz, T., Kührt, E., Palomba, E., Taylor, F.W., Tosi, F., Piccioni, G., Fink, U., Tozzi, G., Barucci, A., Biver, N., Capria, M.-T., Combes, M., Ip, W., Blecka, M., Henry, F., Jacquinod, S., Reess, J.-M., Semery, A., Tiphene, D., 2015. First observations of H2O and CO2 vapor in comet 67P/Churyumov-Gerasimenko made by VIRTIS onboard Rosetta. Astron. Astrophys. 583, A6. doi:10.1051/0004-6361/201526303.

Brown, A.J., Byrne, S., Tornabene, L.L., Roush, T., 2008. Louth crater: evolution of a layered water ice mound. Icarus 196, 433–445.

Brown A., J., Calvin, W.M., P., B., Byrne, S., 2016. Martian north polar cap summer water cycle. Icarus 277, 401–415.

Brown, R.H., Baines, K.H., Bellucci, G., Bibring, J.-P., Buratti, B.J., Capaccioni, F., Cerroni, P., Clark, R.N., Coradini, A., Cruikshank, D.P., Drossart, P., Formisano, V., Jaumann, R., Langevin, Y., Matson, D.L., McCord, T.B., Mennella, V., Miller, E., Nelson, R.M., Nicholson, P.D., Sicardy, B., Sotin, C., 2004. The Cassini visual and infrared mapping spectrometer (Vims) investigation. Space Sci. Rev. 115, 111–168.

Clark, R.N., Cruikshank, D.P., Jaumann, R., Brown, R.H., Stephan, K., Dalle Ore, C.M., Eric Livo, K., Pearson, N., Curchin, J.M., Hoefen, T.M., Buratti, B.J., Filacchione, G., Baines, K.H., Nicholson, P.D., 2012. The surface composition of Iapetus: mapping results from Cassini VIMS. Icarus 218, 831–860.

Collins, G.C., Goodman, J.C., 2007. Enceladus' south polar sea. Icarus 189, 72–82.

Crovisier, J., 1984. The water molecule in comets - Fluorescence mechanisms and thermodynamics of the inner coma. Astro. Astrophy. 130 (2), 361–372.

Debout, V., Bockelée-Morvan, D., Zakharov, V., 2016. A radiative transfer model to treat infrared molecular excitation in cometary atmospheres. Icarus 265, 110–124.

Dhingra, D., Hedman, M.M., Clark, R.N., 2015. Structural diversity of the 3 µ absorption band in Enceladus' plume from Cassini VIMS: insights into subsurface environmental conditions. Div. Planet. Sci. Meeting Abstract# 411.01.

Dhingra, D., Hedman, M.M., Clark, R.N., 2016. Near infrared spectral systematics of Enceladus' plume: links to formation conditions and dominant controls. In: Lunar and Planetary Science Conference, Volume 47 of Lunar and Planetary Science Conference, p. 2638.

Dong, Y., Hill, T.W., Ye, S.-Y., 2015. Characteristics of ice grains in the Enceladus plume from Cassini observations. J. Geophys. Res. Space Phys. 120, 915–937. doi:10.1002/2014JA020288.

Dougherty, M.K., Khurana, K.K., Neubauer, F.M., Russell, C.T., Saur, J., Leisner, S., Burton, M., 2006. Identification of a dynamic atmosphere at Enceladus with the Cassini magnetometer. Science 311, 1406–1409.

Gao, P., Kopparla, P., Zhang, X., Ingersoll, A.P., 2016. Aggregate particles in the plumes of Enceladus. Icarus 264, 227–238.

Goguen, J.D., Buratti, B.J., Brown, R.H., Clark, R.N., Nicholson, P.D., Hedman, M.M., Howell, R.R., Sotin, C., Cruikshank, D.P., Baines, K.H., Lawrence, K.J., Spencer, J.R., Blackburn, D.G., 2013. The temperature and width of an active fissure on Enceladus measured with Cassini VIMS during the 14 April 2012 South Pole flyover. Icarus 226, 1128–1137.

Hansen, C.J., Esposito, L., Stewart, A.I.F., Colwell, J., Hendrix, A., Pryor, W., Shemansky, D., West, R., 2006. Enceladus' water vapor plume. Science 311, 1422–1425.

Hedman, M.M., Gosmeyer, C.M., Nicholson, P.D., Sotin, C., Brown, R.H., Clark, R.N., Baines, K.H., Buratti, B.J., Showalter, M.R., 2013. An observed correlation between plume activity and tidal stresses on Enceladus. Nature 500, 182–184.

Hedman, M.M., Nicholson, P.D., Showalter, M.R., Brown, R.H., Buratti, B.J., Clark, R.N., 2009. Spectral observations of the Enceladus plume with Cassini-vims. Astrophys. J. 693, 1749–1762.

Hobbs, P.V., 1974. Ice Physics. Clarendon Press, Oxford, p. 837.

Hsu, H.-W., Postberg, F., Sekine, Y., Shibuya, T., Kempf, S., Horanyi, M., Juhasz, A., Altobelli, N., Suzuki, K., Masaki, Y., Kuwatani, T., Tachibana, S., Sirono, S.-I., Moragas-Klostermeyer, G., Srama, R., 2015. Ongoing hydrothermal activities within Enceladus. Nature 519, 207–210.

Hurford, T.A., Helfenstein, P., Hoppa, G.V., Greenberg, R., Bills, B.G., 2007. Eruptions arising from tidally controlled periodic openings of rifts on Enceladus. Nature 447, 292–294.

Iess, L., Stevenson, D.J., Parisi, M., Hemingway, D., Jacobson, R.A., Lunine, J.I., Nimmo, F., Armstrong, J.W., Asmar, S.W., Ducci, M., Tortora, P., 2014. The gravity field and interior structure of Enceladus. Science 344, 78–80.

Ingersoll, A.P., Ewald, S.P., 2011. Total particulate mass in Enceladus plumes and mass of Saturn's E ring inferred from Cassini ISS images. Icarus 216, 492–506. doi:10.1016/j.icarus.2011.09.018.

Kempf, S., Schmidt, J., Srama, R., Postberg, F., Spahn, F., Horanyi, M., 2010. Enceladus Dust production - new insights from Cassini. AGU Fall Meeting Abstract# A1562.

Kempf, S., Beckmann, U., Moragas-Klostermeyer, G., Postberg, F., Srama, R., Economou, T., Schmidt, J., Spahn, F., Grün, E, 2008. The E ring in the vicinity of Enceladus. I. Spatial distribution and properties of the ring particles. Icarus 193, 420–437.

Kiefer, S.W., Lu, X., Bethke, C.M., Spencer, J.R., Marshak, S., Navrotsky, A., 2006. A clathrate reservoir hypothesis for Enceladus' south polar plume. Science 314, 1764.

Kouchi, A., Yamamoto, T., Kozasa, T., Kuroda, T., Greenberg, J.M., 1994. Conditions for condensation and preservation of amorphous ice and crystallinity of astrophysical ices. A A 290, 1009–1018.

Mastrapa, R.M., et al., 2008. Optical constants of amorphous and crystalline H2O-ice in the near infrared from 1.1 to 2.6 µm. Icarus 197, 307–320.

Mastrapa, R.M., Sandford, S.A., Roush, T.L., Cruikshank, D.P., Dalle Ore, C.M., 2009. Optical constants of amorphous and crystalline H2O-ice: 2.5-22 µm (4000-455 cm^{-1}) optical constants of H2O-ice. Astrophys. J. 701, 1347–1356.

Nicholson, P.D., Hedman, M.M., Clark, R.N., Showalter, M.R., Cruikshank, D.P., Cuzzi, J.N, Filacchione, G., Capaccioni, F., Cerroni, P., Hansen, G.B., Sicardy, B., Drossart, P., Brown, R.H., Buratti, B.J., Baines, K.H., Coradini, A., 2008. A close look at Saturn's rings with Cassini VIMS. Icarus 193, 182–212.

Nimmo, F., Spencer, J.R., Pappalardo, R.T., Mullen, M.E., 2007. Shear heating as the origin of the plumes and heat flux on Enceladus. Nature 447, 289–291.

Nimmo, F., Porco, C., Mitchell, C., 2014. Tidally Modulated eruptions on enceladus: Cassini ISS observations and models. Astronom. J. 148, 46.

Porco, C., DiNino, D., Nimmo, F., 2014. How the geysers, tidal stresses, and thermal emission across the South Polar Terrain of Enceladus are related. Astronom. J. 148, 45.

Porco, C.C., Helfenstein, P., Thomas, P.C., Ingersoll, A.P., Wisdom, J., West, R., Neukum, G., Denk, T., Wagner, R., Roatsch, T., Kiefer, S., Turtle, E., McEwen, A., Johnson, T.V., Rathbun, J., Veverka, J., Wilson, D., Perry, J., Spitale, J., Brahic, A., Burns, J.A., DelGenio, A.D., Dones, L., Murray, C.D., Squyres, S., 2006. Cassini observes the active South Pole of Enceladus. Science 311, 1393–1401.

Postberg, F., Kempf, S., Hillier, J.K., Srama, R., Green, S.F., McBride, N., Grüna, E., 2008. The E-ring in the vicinity of Enceladus: II. Probing the moon's interior—The composition of E-ring particles. Icarus 193, 438–454.

Postberg, F., Schmidt, J., Hillier, J., Kempf, S., Srama, R., 2011. A salt-water reservoir as the source of compositionally stratified plume on Enceladus. Nature 474, 620–622.

Roberts, J.H., Stickle, A.M., 2014. A recent ocean or sea on Enceladus. AGU Fall Meeting Abstract #P51F-08.

Roberts, J.H., Stickle, A.M., 2015. Impact heating and the South Polar thermal anomaly on Enceladus. In: 46th Lunar and Planetary Science Conference Abstract # 1832.

Schmidt, J., Brilliantov, N., Spahn, F., Kempf, S., 2008. Slow dust in Enceladus' plume from condensation and wall collisions in tiger stripe fractures. Nature 451, 685–688.

Smith-Konter, B., Pappalardo, R.T., 2008. Tidally driven stress accumulation and shear failure of Enceladus's tiger stripes. Icarus 198, 435–451.

Spahn, F., et al., 2006. Cassini dust measurements at Enceladus and implications for the origin of the E-Ring. Science 311, 1416–1418.

Spencer, J.R., Nimmo, F., 2013. Enceladus: an active ice world in the Saturn system. Annu. Rev. Earth Planet. Sci. 41, 693–717.

Spencer, J.R., Pearl, J.C., Segura, M., Flasar, F.M., Mamoutkine, A., Romani, P., Buratti, B.J., Hendrix, A.R., Spilker, L.J., Lopes, R.M.C., 2006. Cassini encounters Enceladus: background and the discovery of a South Polar hot spot. Science 311, 1401–1405.

Spitale, J.N., Porco, C.C., 2007. Association of the jets of Enceladus with the warmest regions on its south-polar fractures. Nature 449, 695–697.

Vahidinia S., J.N. Cuzzi, M.M. Hedman, B. Draine, R.N. Clark, T. Roush, G. Filacchione, P.D. Nicholson, R.H. Brown, B.J. Buratti, C. Sotin.2011 Saturn's F ring grains: aggregates made of crystalline water ice, *Icarus*, 215, 682–694

Waite Jr, J.H., Combi, M.R., Ip, W.-H., Cravens, T.E., McNutt, R.L., Kasprzak, W., Yelle, R., Luhmann, J., Niemann, H., Gell, D., Magee, B., Fletcher, G., Lunine, J., Tseng, W.-L., 2006. Cassini ion and neutral mass spectrometer: Enceladus plume composition and structure. Science 311, 1419–1422.

Ye, S.-Y., Gurnett, D.A., Kurth, W.S., 2016. In-situ measurements of Saturn's dusty rings based on dust impact signals detected by Cassini RPWS. Icarus 279, 51–61.